nature geoscience

Article

https://doi.org/10.1038/s41561-023-01365-2

Geomorphic controls on the abundance and persistence of soil organic carbon pools in erosional landscapes

Received: 20 December 2022

Accepted: 19 December 2023

Published online: 29 January 2024

Check for updates

Brooke D. Hunter [1] ✉, Joshua J. Roering [1], Lucas C. R. Silva [2,3] & Kimber C. Moreland [4]

Soils play a central role in the global carbon cycle and constitute a key component of natural climate solutions that require quantitative predictions of soil organic carbon (SOC) dynamics at local to regional scales. In hilly and mountainous terrain, variations in uplift and stream incision generate gradients in erosion and hillslope morphology that control soil properties that impact the abundance and persistence of SOC. Here we use topographic and soil biogeochemical analyses to show that across 16 sites in our study region, total SOC stocks and the typically slower-cycling mineral-associated fraction of SOC decrease exponentially with modelled erosion rate from 21.0 to 0.2 kg m^{-2} and 12.0 to 0.1 kg m^{-2}, respectively. Along the greater than order-of-magnitude erosional gradient, radiocarbon ($\Delta^{14}C$), soil thickness and texture data trend younger, thinner and coarser, respectively, such that fast-eroding sites have much less SOC than slow-eroding sites and are dominated by faster-cycling SOC pools. By coupling these erosion-driven soil and SOC trends with high-resolution topographic data, hilltop convexity and other erosion rate metrics can be readily applied to estimate SOC abundance and persistence in diverse landscape settings, facilitating our ability to predict carbon dynamics across a range of spatiotemporal scales.

With ~2,400 Pg of organic carbon (OC) in the upper 2 m depth[1,2], soils are the largest terrestrial store of OC, holding more OC than vegetation and the atmosphere combined[3–6], with some soil organic compounds persisting for millennia[7–10]. Given the critical role of soil organic carbon (SOC) in the carbon cycle, the use of SOC in climate solutions[11–13] and Earth system models has been emphasized in recent syntheses[11,13,14]. Despite the pressing importance of understanding SOC stocks, our ability to estimate and predict SOC at regional and local scales relevant for policy and management is lacking, at least in part, because topographic variations preclude extrapolation of localized SOC soil pit data across erosional landscapes. In particular, SOC stocks in hilly and mountainous terrain, such as the western United States, are strongly modulated by soil properties, including thickness, texture and weathering intensity[15,16]. Systematic trends in these pedogenic characteristics result from feedbacks between base-level lowering and hillslope evolution, soil transport, production and weathering over >1,000 yr timescales. In these erosional settings, the interplay of uplift and incision with hillslope processes generates a geomorphic template on which integral biological and ecological processes regulate organic matter supply as well as SOC persistence[15,17,18]. Quantifying the linkages between landscapes and soil properties is imperative to understanding global SOC stocks and persistence (and soil as a climate change solution) given

[1]Department of Earth Sciences, University of Oregon, Eugene, OR, USA. [2]Environmental Studies Program, University of Oregon, Eugene, OR, USA. [3]Department of Biology, Institute of Ecology and Evolution, University of Oregon, Eugene, OR, USA. [4]Center for Accelerator Mass Spectrometry, Lawrence Livermore National Laboratory, Livermore, CA, USA. ✉e-mail: bhunter2@uoregon.edu

https://doi.org/10.1038/s41561-023-01365-2

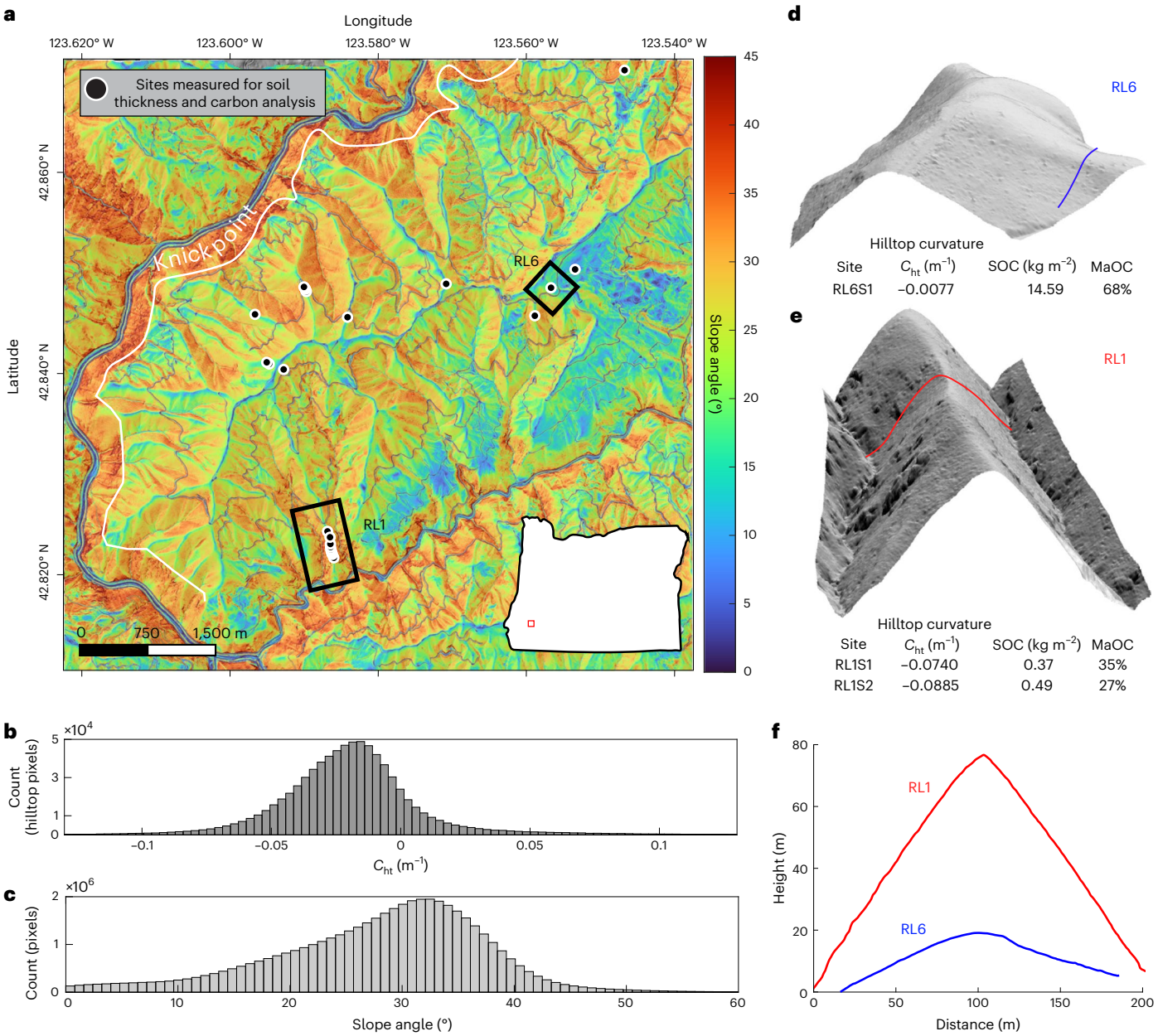

Fig. 1 | Study area. a, Slope map (degrees) of Rabbit Mountain in the Cow Creek recreation area. Soil sampling locations at hilltops along ridgelines are shown as black dots. Insets RL6 and RL1 correspond to **d** and **e**, respectively (Extended Data Fig. 1). **b**, Distribution of hilltop curvature (C_{ht}) values extracted along ridgelines (Extended Data Fig. 1). **c**, Distribution of hillslope angles across the whole landscape calculated across a smoothed 10 m DEM. **d**, Hillshade of RL6 site. Slopes are gentle, and SOC stocks are higher. Blue line represents the ridgeline transect in **f**. RL6S1 was taken along ridgeline perpendicular to blue transect. **e**, Hillshade of RL1 site. Slopes are steep and rocky with sharp hilltops. SOC stocks are low. Red line represents the ridgeline transect in **f**. RL1S1–RL1S10 were taken along ridgeline perpendicular to red transect. **f**, Transects of the ridgelines RL1 (red) and RL6 (blue). RL1 has steep slopes with a convex hilltop, while RL6 is broader and gentler.

that over 60% of the Earth land surface is composed of landscapes with a slope greater than 8% (ref. 19).

The persistence of SOC pools reflects biogeochemical and ecological properties, such as microbial activity and net primary production, that regulate organic matter turnover and accumulation or loss over time[20,21]. Despite a multitude of studies, controls on SOC persistence and accumulation can be difficult to define[9,22,23]. Operationally, the persistence or turnover in SOC pools can be inferred directly from radiocarbon data as well as the proportions of particulate organic carbon (POC) and mineral-associated organic carbon (MaOC), where POC tends to be relatively short lived (decades to centuries) while MaOC tends to persist longer (centuries to millennia) on average[8,10,22]. POC is often found to consist primarily of plant-derived organic matter that is either unprotected ('free' POC) or physically shielded from decomposition via occlusion in soil aggregates. MaOC is often composed of smaller, simpler carbon compounds that include organo-mineral associations through adsorption of OC onto mineral surfaces. Microbial processing of organic matter can lead to the formation of soil aggregates from organo-mineral complexes, such as those formed from microbial interactions with pedogenic oxides[10,24], which render MaOC more stable than POC[9,25–28]. As a result of these contrasts in primary protection mechanisms and inherent structure, POC pools tend to have relatively younger average radiocarbon ^{14}C ages[7,9] compared with MaOC pools. Thus, the relative abundances of POC and MaOC pools

https://doi.org/10.1038/s41561-023-01365-2

Table 1 | Individual site data

Site	Soil thickness (cm)	C_{ht} (m^{-1})	Modelled E ($mm\ yr^{-1}$)	SOC ($kg\ m^{-2}$)	MaOC ($kg\ m^{-2}$)	POC ($kg\ m^{-2}$)	MaOC% of total stock
RL1S3	0	−0.1011	0.2021				
RL1S4	0	−0.0956	0.1911				
RL1S5	0	−0.0937	0.1873				
RL1S2	12.5	−0.0885	0.1771	0.49	0.12	0.34	26.6
RL1S6	10	−0.0820	0.1639				
RL1S1	8	−0.0740	0.1480	0.37	0.13	0.23	35.4
RL2S3	23	−0.0708	0.1416	3.33	1.08	2.15	33.5
RL5S1	10	−0.0625	0.1251	1.74	0.67	1.28	34.5
RL2S5	12	−0.0610	0.1220				
RL2S6	7	−0.0527	0.1054				
RL2S1	25	−0.0518	0.1036	2.14	0.86	1.19	41.9
RL1S7	0	−0.0460	0.0921				
NRS1A	35	−0.0440	0.0880	1.54			
RL2S4	10	−0.0435	0.0870	0.96	0.31	0.48	39.0
RL1S8	18	−0.0381	0.0761				
NRS5	62	−0.0371	0.0742	4.18	2.50	2.08	54.7
T3S1	46	−0.0319	0.0639	3.94	1.56	1.32	54.2
BR1S4A	65	−0.0310	0.0620	4.55	2.59	2.04	55.9
RL1S9	27	−0.0278	0.0555	5.83	1.65	3.69	30.9
RL7S1	11	−0.0276	0.0551	1.88	0.91	0.79	53.5
RL1S10	20	−0.0252	0.0505				
RL3S1	200	−0.0155	0.0309	14.87	9.18	5.49	62.6
T1S2	125	−0.0086	0.0173	9.07	4.60	3.58	56.2
RL6S1	120	−0.0077	0.0154	14.59	10.73	4.88	68.7
RL4S1	138	−0.0038	0.0077	21.78	12.09	7.54	61.6

Site soil thickness measurements and C_{ht}, E, SOC, MaOC and POC stock calculations ordered by increasing convexity, higher $|C_{ht}|$. Standard deviation values of C_{ht} were calculated from hilltop values located in a 5×5 m area around the pit location (~8–10 ridgeline pixels). Precision for OC% determined by replication of ten soil standards is 0.035 s.d. Standard deviations of duplicated OC% values are located in Supplementary Table 2.

across landscapes provide a critical constraint for SOC inventories and simulations of carbon cycling[8].

The thickness and weathering intensity of soils are determined by erosion rate via the balance of soil production and transport and influence soil residence time and SOC storage in two critical ways: First, the thickness of soil (defined here as the layer of mixed or disaggregated material that lacks relic rock structure) varies inversely with erosion rate according to field-based studies and process-based geomorphic models[29]. As such, soil thickness sets the accommodation space available for SOC storage such that thicker soils have greater capacity given an ample supply of organic matter[30,31]. Second, the intensity of soil weathering due to biological and chemical alteration depends on the mean soil residence time, which varies inversely with erosion rate[30–32]. As such, slow-eroding, thick soils feature longer mean soil particle residence times and thus increased exposure to chemical alteration, resulting in finer-textured soils with an abundance of pedogenic minerals that facilitate SOC stabilization mechanisms through the creation of minerals with high reactive surface area[17]. In particular, many studies have shown strong correlations between SOC and clay content, and particularly pedogenic oxide minerals[10,16,33,34].

Previous studies have successfully utilized high-resolution topographic data to connect morphologic metrics, such as local curvature, with soil thickness and SOC stocks to generate highly accurate predictions of SOC storage within an individual catchment[15,30,35]. Another recent investigation explored geomorphic and geochemical controls on total SOC and operational pools, although the results were limited due to small sample size and narrow variation in erosion rate[17], precluding the utility for landscape-scale predictions. As a result, we lack a conceptual framework and field observations that define how variations in erosion rate and hillslope morphology driven by the long-term pattern of uplift and incision control soil properties and the abundance and persistence of total SOC, MaOC and POC pools across a range of scales.

Hilltop curvature as an erosion rate proxy

In this study, we demonstrate that erosion rate, which can be modelled using high-resolution topography and calibrated geomorphic process models[36–39], serves as a first-order control on not only total SOC, but also MaOC and POC pools and SOC persistence derived from radiocarbon analysis. We focus our topographic analysis and field sampling along ridgelines in the Klamath Mountains of southwestern Oregon that vary from broad and gentle to narrow and extremely steep. To quantify spatial variations in erosion rate, we used airborne lidar to calculate and map hilltop convexity (C_{ht}) across a 1 m digital elevation model (DEM), which serves as an erosion rate proxy that emerges by coupling a soil mass conservation equation and transport model that was proposed >100 years ago and is supported by numerous field studies[36,40]. The C_{ht} measured along ridgelines reflects catchment-scale erosion rates and hillslope form set by the balance of long-term uplift and incision. Sharp, high-convexity ridgelines with faster erosion rates are associated with steeper hillslopes and thin, coarse soils. Broad, less convex ridgelines with

https://doi.org/10.1038/s41561-023-01365-2

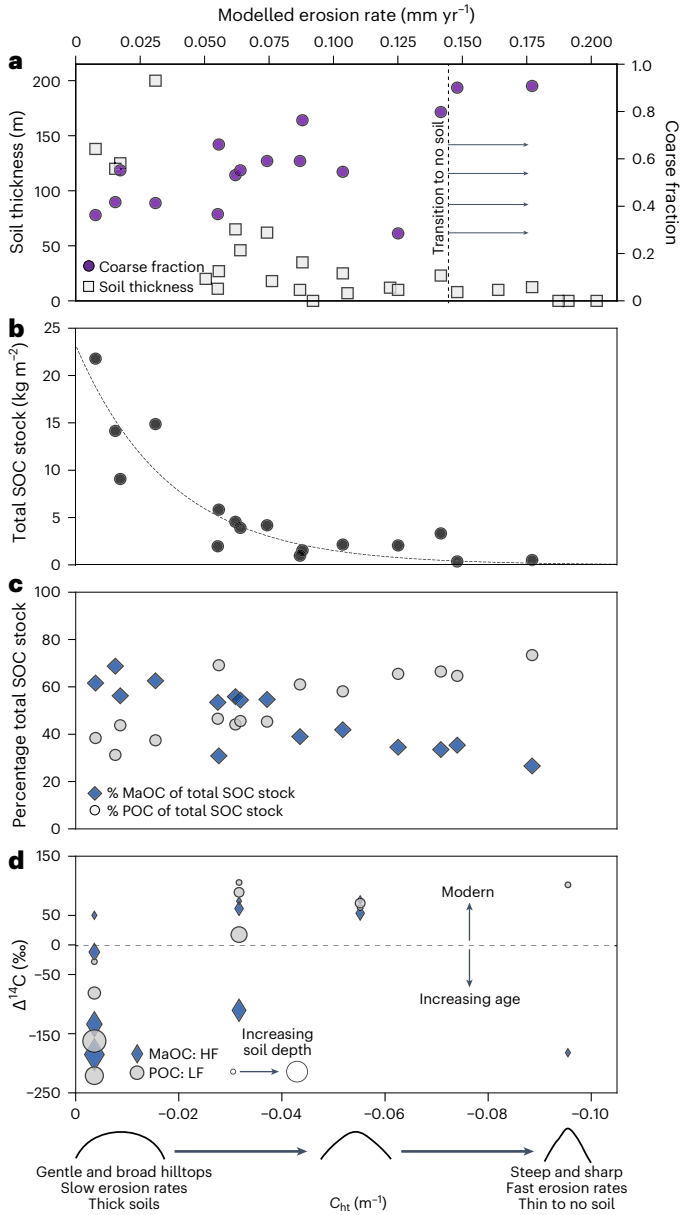

Fig. 2 | Total SOC, percentage MaOC and POC stock, fraction modern, soil thickness and coarse fraction as functions of C_{ht} and modelled E. **a**, Depth-weighted coarse fraction, f_c (mass of soil >2 mm divided by total mass of sample collected), increases with sharper, more-negative C_{ht} and increasing E. As soils become more clast rich, soil thickness (grey squares) decreases, providing less accommodation depth for SOC storage. **b**, Total SOC stock decreases with C_{ht} as faster-eroding soils produce shallow, rocky, relatively unweathered soils. SOC stock = 23.4 × 10−55.0C_{ht} (r^2 = 0.85). **c**, Percentage of total stock that is MaOC (blue diamonds), measured in the <53 µm fraction, decreases with erosion rate (more-negative C_{ht} and increasing E). MaOC stock = 14.7 × 10−62.3C_{ht} (r^2 = 0.83). MaOC stock comprises most of the total SOC stock (~60–70%) at the slowest sites and decreases to <35% at the fastest sites. Although the total POC stock, measured as the 53–2,000 µm fraction, also decreases with faster erosion rates, it does not do so at the same rate. POC becomes the dominate fraction as erosion rate increases (grey circles). POC stock = 7.4×10−39.52C_{ht} (r^2 = 0.72). **d**, $\Delta^{14}C$ (‰) values for MaOC (blue diamonds) and POC (grey circles), measured on the density separated samples, at selected sites across erosion rate gradient. Increasing sizes of data points represent deeper soil samples. Deeper samples typically have lower fraction modern values, while surface samples are modern.

slower erosion rates are associated with gentle slopes and thicker, more weathered soils. To link soil properties and SOC stocks to erosion rate, we model erosion rate, E, using C_{ht}, a soil transport rate coefficient (K) of 0.004 m^2 yr^{-1} and a rock/soil bulk density ratio (ρ_r/ρ_s) of 2.0 (refs. 38,39).

$$E = \frac{-C_{ht} \times K}{(\rho_r/\rho_s)} \quad (1)$$

In our southwestern Oregon study area, a prominent knickzone revealed by stark contrasts in hilltop morphology separates broad, gentle slopes (slow-eroding) and sharp, steep slopes (fast-eroding) terrain (Fig. 1 and Extended Data Fig. 1) across a multitude of forested, hilly and mountainous watersheds. The region is characterized by warm, dry summers and cool, wet winters with annual precipitation of ~100 cm falling predominantly from October to May[41]. The vegetation is dominated by Douglas fir (*Pseudotsuga menziesii* (Mirbel) Franco), which is homogeneous across our sampling sites[42]. The region is underlain by marine sedimentary rocks and volcanics that resulted from tectonic accretion[41]. Catchments below the knickzone exhibit sharp hilltops (C_{ht} values are typically <−0.05 m^{-1} and E > 0.1 mm yr^{-1}) and steep (>35°) slopes, with thin, coarse and relatively unaltered soils. These soils contrast with those collected from catchments situated above the knickzone that have yet to experience increased erosion associated with the upstream propagating wave of incision. Above the knickzone, we observe broad hilltops (curvature values are typically <0.015 m^{-1} and E < 0.03 mm yr^{-1}) with thick, well-developed soils containing abundant silt and clay and pedogenic minerals.

Soil properties and organic carbon vary with erosion rate

To quantify the strong contrast in hilltop form across our sites, we use a scale-dependent approach (Methods) for estimating C_{ht} (and thus E) that accounts for the decreasing length scale of curvature estimation required to avoid bias as hilltops become sharper (more convex)[37]. Nonetheless, our observed trends between E and SOC, MaOC and POC persist if all sites are analysed using a common wavelet scale; thus, our results are robust to the choice of scale (Extended Data Fig. 2). We sampled soils along hilltops with modelled erosion rates (E) from <0.01 to >0.19 mm yr^{-1} to capture the range of erosion rate and topographic variability in the region (Extended Data Fig. 1). We determined the relationship between soil thickness (measured from soil pits and augers) and C_{ht} at 25 hilltop locations and collected soil profiles for carbon and nitrogen analysis at 16 of these sites (Table 1). In each pit, we sampled the soil profile for bulk density and laboratory analyses approximately every 5 cm (Supplementary Table 1), and auger samples were collected in ~10 cm increments. In the laboratory, we oven dried and sieved soil into the fine fraction, f_f (<2 mm), and coarse fraction, f_c (>2 mm). We used a ball mill to homogenize aliquots of fine-fraction soil to manually encapsulate powdered material in tin capsules (sample size approximately 10–100 mg) (ref. 43). We measured OC% on a mass basis through combustion and gas chromatography in a FlashSmart elemental analyser (Thermo Fisher Scientific). SOC density (gC cm^{-3}) for each sample was calculated using total bulk density, ρ_{total} (total grams of sample, including f_f and f_c, per cm^3), a mass-based coarse-fraction correction ($1 - f_c$) and the OC% (percentage mass C in f_f material) as described in refs. 17,44.

$$\text{SOC density} = 0.01 \times \text{OC\%} \times \rho_{total} \times (1 - f_c) \quad (2)$$

As expected, OC% and SOC density (kg m^{-3}) both decrease with depth for nearly all sites (Extended Data Fig. 3)[10,15,31]. Across similar depths, OC% values do not vary systematically with C_{ht} and modelled erosion rate. However, the depth-averaged coarse fraction, f_c, is strongly correlated with erosion rate, varying from 0.25 on slow-eroding sites to >0.75 on fast-eroding sites (Fig. 2a and Extended Data Fig. 4). As a result, SOC density decreases systematically with increasing erosion rate across similar depths. This finding demonstrates that although the OC%

https://doi.org/10.1038/s41561-023-01365-2

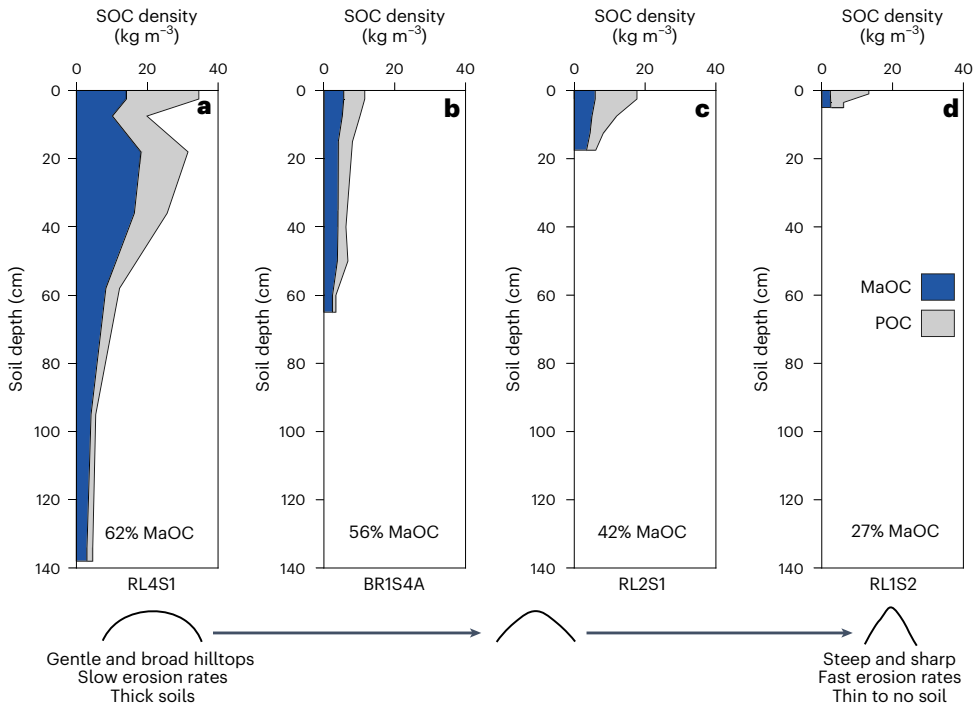

Fig. 3 | SOC profiles. Four selected MaOC (blue) and POC (grey) density (kg m^{-3}) profiles (all sites presented in Extended Data Fig. 5) that increase in erosion rate from left to right. **a**, RL4S1 is the slowest of the four sites selected, with a curvature of about −0.0038, and has a total SOC stock (kg m^{-2}) made up of 62% MaOC. POC density is highest at the surface and declines with depth. Soils are also thicker at the slow-eroding sites, allowing for more accommodation space and storage capacity compared with shallow, rockier sites. **b**, Site BR1S4A is made up of ~56% MaOC. **c**, At site RL2S1, POC becomes the dominant fraction with 58%. **d**, RL1S2 is one of the fastest sites; curvature is −0.0885, and POC stock makes up ~73% of the total SOC stock.

of the fine fraction on both fast- and slow-eroding sites does not vary markedly, the explicit consideration of soil thickness and coarse clast fraction reveals strong erosional controls in SOC density and stocks.

MaOC and POC can be separated by size or density (1.6–1.85 g cm^{-3}) (ref. 22), where POC consists of the larger (53–2,000 µm) or the light fraction (LF), while MaOC is composed of the clay- and silt-sized material (<53 µm) or the heavy fraction (HF). To measure how the total and relative abundance of each SOC pool varies with modelled erosion rate, we separated soil samples by size into POC and MaOC fractions with the 53 µm threshold[22,45]. To disaggregate the fine-fraction soil, samples were shaken overnight on an oscillating table with sodium hexametaphosphate, wet sieved at 53 µm and oven dried at 60° C for 24–36 h. We then crushed samples manually and encapsulated them in tin capsules to determine carbon concentrations on a mass basis as described in the preceding. MaOC and POC densities were calculated as follows:

$$\text{MaOC density} = 0.01\times \text{OC}\%\times\rho_{\text{total}}\times\left(1-f_{\text{c}}\right)\times\left(1-f_{\geq 53}\right) \quad (3)$$

$$\text{POC density} = 0.01\times \text{OC}\%\times\rho_{\text{total}}\times\left(1-f_{\text{c}}\right)\times\left(1-f_{<53}\right) \quad (4)$$

where $f_{\geq 53}$ (grams of soil ≥53 µm divided by grams of fine-fraction mass) and $f_{<53}$ (grams of soil <53 µm divided by grams of fine-fraction mass) are mass correction factors.

Similar to total SOC, MaOC and POC concentrations and densities tend to decrease with depth across all sites (Fig. 3 and Extended Data Fig. 5). Slow-eroding sites (small C_{ht} values close to zero) have deeper soil profiles with abundant MaOC (Fig. 3a). Consistent with other studies, POC density is highest at the surfaces and steadily declines with depth[17,46] such that the majority of SOC in deeper horizons is contained within the MaOC fraction. Our data show that both total SOC (Fig. 2b) and MaOC stocks decrease exponentially with faster erosion rates. At the slowest-eroding sites ($|C_{\text{ht}}| < 0.009$ m^{-1}), total SOC stocks range from 9.1 to 21.8 kg m^{-2} and decrease to 0.4–3.3 kg m^{-2} at the fastest-eroding sites ($|C_{\text{ht}}| > 0.7$ m^{-1}). MaOC values follow a similar pattern, making up ~55–70% of the total SOC at the slowest sites and less than 35% at the fastest (Fig. 2c). POC stocks also decline with modelled erosion rate from 3.6–7.5 kg m^{-2} to 0.23–2.15 kg m^{-2}, although they exhibit less variation across our sites. Notably, however, the fraction of the total SOC stock that consists of POC increases with erosion rate, constituting >70% of the total stock in rapidly eroding sites (Fig. 2c).

Importantly, the abundance of MaOC at our fast-eroding sites may be overestimated (while POC is underestimated). In coarser soils, the fine-fraction POC (particulate organic material <53 µm) may contribute a greater proportion to the <53 µm fraction interpreted as our MaOC fraction, when compared with finer-textured soils. This systemic bias could inflate MaOC carbon content values through the introduction of higher carbon content material at our fast-eroding sites. Nonetheless, our size segregation approach is robust. When we compared the sum of our MaOC and POC stock values with our total measured SOC stock, the sum of the fractions is consistent (within 15%) with total SOC for all but two of the sites (Supplementary Table 1).

Radiocarbon analysis of soil organic carbon pools

To quantify variation in the persistence of MaOC and POC pools with erosion rate, we generated radiocarbon data for a subset of our samples by elemental analyser accelerator mass spectrometry (EA-AMS) at the National Ocean Sciences Accelerator Mass Spectrometry facility. We measured ^{14}C for the MaOC and POC pools after density separation, rather than size separation, using a sodium polytungstate solution with a density of 1.85 g cm^{-3}. We calculated age-corrected Δ^{14}C (‰), the difference in the ratio of ^{14}C to stable ^{12}C in a sample compared to reference material, corrected to the date of collection in accordance with standard conventions[47] for both pools in four selected sites (Fig. 2d), where more-depleted values are indicative of older,

slower-cycling OC, and less-depleted values represent younger, faster-cycling OC on average (Supplementary Table 4). Consistent with expectations[48], we found progressively older SOC with depth as $\Delta^{14}C$ values decrease from modern to <−150 ‰. Our slowest erosion site (RL4S1) has older (more-depleted) $\Delta^{14}C$ values for both the MaOC and POC pools compared with faster sites. At this slow site, some POC values are slightly older (more-depleted $\Delta^{14}C$ values) than MaOC values, which could reflect POC protection by occlusion in stable macro aggregates and/or less microbial activity at depth. At a moderate-eroding site BR1S4A (C_{ht} = −0.031 m^{-1} and E = 0.062 mm yr^{-1}), the POC fraction is on average younger than MaOC for a given depth. Near the surface, both MaOC and POC have modern $\Delta^{14}C$ values, but in the 55–65 cm interval, MaOC decreases to −110‰ while POC remains modern. Most generally, as erosion rate increases, $\Delta^{14}C$ trends towards younger (less-depleted $\Delta^{14}C$ values) values on average, suggesting fresh organic matter input and a faster cycling rate.

One notable exception to these radiocarbon trends is at our fastest-eroding site (RL1S2, C_{ht} = −0.089 m^{-1} and E = 0.19 mm yr^{-1}), where our MaOC $\Delta^{14}C$ value is relatively old. We collected this shallow sample (5–10 cm) from rooted seams within fractured rock close to the surface. The site is dominated by POC, demonstrated by both size and density separation methods, and the MaOC is composed primarily of sand-sized clasts. From field observations, we note that there are fewer fine roots and abundant coarse roots at this site. At these fast-eroding sites (coincident with the 'no soil' transition in Fig. 1a), soil properties are probably not conducive to fresh organic matter being readily incorporated into the soil. The coarse-rock-dominated soil ecosystems at these fast-eroding sites are well drained and relatively dry, probably with reduced microbial activity. Since radiocarbon measurements reflect an ensemble of SOC ages, it is possible this older age (more-depleted values) that deviates from the erosional trend reflects less fast-cycling carbon and fresh organic matter incorporation into the MaOC fraction compared with slower sites. The limited incorporation of fresh organic matter would result in older ^{14}C (more-depleted material) having a greater influence on the average values we measure. This implies that in addition to soil thickness and coarse-fraction content, erosion rate may influence other soil formation factors such as soil moisture and microbial activity that affect the incorporation of and persistence of SOC[49].

Landscape control on soil properties and organic carbon

Our field observations in combination with geomorphic theory demonstrate that fast-eroding sites with steep slopes and sharp hilltops have shallow coarse soils with inferred short particle residence times that feature minimal alteration. By contrast, slow-eroding sites allow for long mean residence times with thick, highly altered soils. Although fast-eroding sites show higher OC% in the f_f, accounting for coarse fraction and depth indicates that slower sites have larger SOC density and stocks. At rapidly eroding sites, not only do thin soils with high coarse-fraction content have less accommodation space for SOC storage, but the relatively unaltered material limits mineral association of SOC and favours a greater fraction of POC (which produces the higher OC% values). Given the abundance of studies that demonstrate the association of MaOC with slow turnover of SOC and our radiocarbon measurements, these findings suggest that erosion rate and hillslope form regulate not only SOC stocks but also SOC persistence in hilly and mountainous settings.

While the characterization of biotic processes and shorter timescale properties, including the redistribution of SOC through erosion[50], is crucial for SOC cycling[21], spatial variations in hillslope form driven by differential uplift and incision play an integral role in setting erosion rates and soil properties on which biogeochemical processes are superimposed. Our results demonstrate that these landscape-scale interactions impart key controls on SOC stocks, pool abundance and persistence. The emergence of readily available high-resolution topographic data has enabled the quantification of erosional metrics for integration with soil carbon models. This underutilized linkage affords the identification of terrain for SOC storage potential and the improvement of baseline carbon drawdown predictions that inform climate change mitigation and adaptation across a range of scales.

Online content

Any methods, additional references, Nature Portfolio reporting summaries, source data, extended data, supplementary information, acknowledgements, peer review information; details of author contributions and competing interests; and statements of data and code availability are available at https://doi.org/10.1038/s41561-023-01365-2.

References

1. Batjes, N. H. Total carbon and nitrogen in the soils of the world. *Eur. J. Soil Sci.* **47**, 151–163 (1996).
2. Friedlingstein, P. et al. Global carbon budget 2020. *Earth Syst. Sci. Data* **12**, 3269–3340 (2020).
3. Jobbágy, E. G. & Jackson, R. B. The vertical distribution of soil organic carbon and its relation to climate and vegetation. *Ecol. Appl.* **10**, 423–436 (2000).
4. Kirschbaum, M. U. F. Will changes in soil organic carbon act as a positive or negative feedback on global warming? *Biogeochemistry* **48**, 21–51 (2000).
5. Le Quéré, C. et al. Global carbon budget 2014. *Earth Syst. Sci. Data* **7**, 47–85 (2015).
6. Tarnocai, C. et al. Soil organic carbon pools in the northern circumpolar permafrost region. *Glob. Biogeochem. Cycles* https://doi.org/10.1029/2008GB003327 (2009).
7. Trumbore, S. Age of soil organic matter and soil respiration: radiocarbon constraints on belowground C dynamics. *Ecol. Appl.* **10**, 399–411 (2000).
8. Lehmann, J. & Kleber, M. The contentious nature of soil organic matter. *Nature* **528**, 60–68 (2015).
9. von Lützow, M. et al. SOM fractionation methods: relevance to functional pools and to stabilization mechanisms. *Soil Biol. Biochem.* **39**, 2183–2207 (2007).
10. Schrumpf, M., Kaiser, K., Mayer, A., Hempel, G. & Trumbore, S. Age distribution, extractability, and stability of mineral-bound organic carbon in central European soils. *Biogeosciences* **18**, 1241–1257 (2021).
11. Bossio, D. A. et al. The role of soil carbon in natural climate solutions. *Nat. Sustain.* https://doi.org/10.1038/s41893-020-0491-z (2020).
12. Jungkunst, H. F., Göpel, J., Horvath, T., Ott, S. & Brunn, M. Global soil organic carbon–climate interactions: why scales matter. *Wiley Interdiscip. Rev. Clim. Change* https://doi.org/10.1002/wcc.780 (2022).
13. Longbottom, T. et al. What's soil got to do with climate change? *GSA Today* **32**, 4–10 (2022).
14. Walker, W. S. et al. The global potential for increased storage of carbon on land. *Proc. Natl Acad. Sci. USA* **119**, e2111312119 (2022).
15. Patton, N. R., Lohse, K. A., Seyfried, M. S., Godsey, S. E. & Parsons, S. B. Topographic controls of soil organic carbon on soil-mantled landscapes. *Sci. Rep.* **9**, 6390 (2019).
16. Lawrence, C. R., Schulz, M. S., Masiello, C. A., Chadwick, O. A. & Harden, J. W. The trajectory of soil development and its relationship to soil carbon dynamics. *Geoderma* **403**, 115378 (2021).
17. Wang, X. et al. Storage and export of soil carbon and mineral surface area along an erosional gradient in the Sierra Nevada, California. *Geoderma* **321**, 151–163 (2018).
18. Yoo, K. et al. Evolution of hillslope soils: the geomorphic theater and the geochemical play. *Appl. Geochem.* **26**, S149–S153 (2011).

19. Staub, B., Rosenzweig, C. & Rind, D. *Global Digital Data Sets of Soil Type, Soil Texture, Surface Slope, and Other Properties: Documentation of Archived Data Tape* (NASA, 1987).
20. Schmidt, M. W. I. et al. Persistence of soil organic matter as an ecosystem property. *Nature* **478**, 49–56 (2011).
21. Doetterl, S. et al. Links among warming, carbon and microbial dynamics mediated by soil mineral weathering. *Nat. Geosci.* **11**, 589–593 (2018).
22. Lavallee, J. M., Soong, J. L. & Cotrufo, M. F. Conceptualizing soil organic matter into particulate and mineral-associated forms to address global change in the 21st century. *Glob. Change Biol.* **26**, 261–273 (2020).
23. Cotrufo, M. F. & Lavallee, J. M. in *Advances in Agronomy* Vol. 172 (ed. Sparks, D. L.) 1–66 (Academic Press, 2022).
24. Silva, L. C. R. et al. Iron-mediated stabilization of soil carbon amplifies the benefits of ecological restoration in degraded lands. *Ecol. Appl.* **25**, 1226–1234 (2015).
25. Blanco-Canqui, H. & Lal, R. Mechanisms of carbon sequestration in soil aggregates. *Crit. Rev. Plant Sci.* **23**, 481–504 (2004).
26. Poeplau, C. et al. Isolating organic carbon fractions with varying turnover rates in temperate agricultural soils—a comprehensive method comparison. *Soil Biol. Biochem.* **125**, 10–26 (2018).
27. Rasmussen, C., Torn, M. S. & Southard, R. J. Mineral assemblage and aggregates control carbon dynamics in a California conifer forest. *Soil Sci. Soc. Am. J.* **69**, 1711–1721 (2005).
28. Totsche, K. U. et al. Microaggregates in soils. *J. Plant Nutr. Soil Sci.* **181**, 104–136 (2018).
29. Heimsath, A. M., Dietrich, W. E., Nishiizumi, K. & Finkel, R. C. The soil production function and landscape equilibrium. *Nature* **388**, 358–361 (1997).
30. Yoo, K., Amundson, R., Heimsath, A. M. & Dietrich, W. E. Spatial patterns of soil organic carbon on hillslopes: integrating geomorphic processes and the biological C cycle. *Geoderma* **130**, 47–65 (2006).
31. Wang, X. et al. Soil organic carbon and mineral interactions on climatically different hillslopes. *Geoderma* **322**, 71–80 (2018).
32. Dixon, J. L. & Riebe, C. S. Tracing and pacing soil across slopes. *Elements* **10**, 363–368 (2014).
33. Torn, M. S., Trumbore, S. E., Chadwick, O. A., Vitousek, P. M. & Hendricks, D. M. Mineral control of soil organic carbon storage and turnover. *Nature* **389**, 170–173 (1997).
34. Hunter, B. D. et al. Pedogenic pathways and deep weathering controls on soil organic carbon in Pacific Northwest forest soils. *Geoderma* **436**, 116531 (2023).
35. Thompson, J. A. & Kolka, R. K. Soil carbon storage estimation in a forested watershed using quantitative soil–landscape modeling. *Soil Sci. Soc. Am. J.* **69**, 1086–1093 (2005).
36. Hurst, M. D., Mudd, S. M., Walcott, R., Attal, M. & Yoo, K. Using hilltop curvature to derive the spatial distribution of erosion rates. *J. Geophys. Res. Earth Surf* **117**, F02017 (2012).
37. Struble, W. T. & Roering, J. J. Hilltop curvature as a proxy for erosion rate: wavelets enable rapid computation and reveal systematic underestimation. *Earth Surf. Dynam.* **9**, 1279–1300 (2021).
38. Roering, J. J., Perron, J. T. & Kirchner, J. W. Functional relationships between denudation and hillslope form and relief. *Earth Planet. Sci. Lett.* **264**, 245–258 (2007).
39. Perron, J. T. Climate and the pace of erosional landscape evolution. *Annu. Rev. Earth Planet. Sci.* **45**, 561–591 (2017).
40. Gilbert, G. K. The convexity of hilltops. *J. Geol.* **17**, 344–350 (1909).
41. Wells, R. E. et al. *Geologic Map and Database of the Roseburg 30′ x 60′ Quadrangle, Douglas and Coos Counties, Oregon* (USGS, 2001); https://doi.org/10.3133/ofr00376
42. Franklin, J. F. & Dryness, C. T. *Natural Vegetation of Oregon and Washington*, (U.S. Government Printing Office, 1973).
43. Wright, J. L. et al. Sixteen hundred years of increasing tree cover prior to modern deforestation in southern Amazon and central Brazilian savannas. *Glob. Change Biol.* **27**, 136–150 (2021).
44. Poeplau, C., Vos, C. & Don, A. Soil organic carbon stocks are systematically overestimated by misuse of the parameters bulk density and rock fragment content. *SOIL* **3**, 61–66 (2017).
45. Cotrufo, M. F., Ranalli, M. G., Haddix, M. L., Six, J. & Lugato, E. Soil carbon storage informed by particulate and mineral-associated organic matter. *Nat. Geosci.* **12**, 989–994 (2019).
46. Jackson, R. B. et al. The ecology of soil carbon: pools, vulnerabilities, and biotic and abiotic controls. *Annu. Rev. Ecol. Evol. Syst.* **48**, 419–445 (2017).
47. Stuiver, M. & Polach, H. A. Discussion Reporting of ^{14}C Data. *Radiocarbon* **19**, 355–363 (1977).
48. Moreland, K. et al. Deep in the Sierra Nevada critical zone: saprock represents a large terrestrial organic carbon stock. *Environ. Res. Lett.* **16**, 124059 (2021).
49. Jenny, H. *Factors of Soil Formation: A System of Quantitative Pedology* (Dover, 1994).
50. Ma, Y. et al. Modelling the whole profile soil organic carbon dynamics considering soil redistribution under future climate change and landscape projections over the Lower Hunter Valley, Australia. *Land* **12**, 255 (2023).

Methods

Organic carbon stock calculations

Total SOC, MaOC and POC stocks were calculated with the integrate.trapz function in the SciPy package[51] in Python. We assigned depth values for the calculated SOC density measurements (equations (2)–(4)) as the centre of the sampled depth interval. However, to ensure we integrated through the entire soil profile, we added rows 'SAMPLE_NAME_0_0' for a zero-depth top sample that mirrored measurements and calculations from the 'SAMPLE_NAME_0_5' values and a 'SAMPLE_NAME_deepest_deepest' at the base of each profile that copies the deepest measured interval.

Hilltop curvature measurements

We calculated curvature across all of Rabbit Mountain using wavelet scales from 5 to 45 m with a 1 m lidar-derived DEM with code created and implemented in ref. 37. These methods utilize functions in TopoToolBox[52]. To get C_{ht} values, we extracted ridgelines with the 'divides' function available in TopoToolbox. To determine C_{ht} values at each site, we calculated the mean curvature and standard deviation within 5 × 5 m kernels around each of our 25 sites.

At each of our 25 sites, we isolated site-specific values, with a mean C_{ht} value within a 5 × 5 m kernel around the soil pit. We selected the C_{ht} value for the smallest wavelet scale where the percentage coefficient of variation calculated with equation (4) in the kernel window was ≤5% (Supplementary Table 1). For sites where pits are located slightly off of mapped divides (~1–5 m deviation), we used the 'snap2stream' function in TopoToolbox to find the closest point along the ridgeline.

$$\text{Percentage coefficient of variation} = 100\times\left(\frac{\text{standard deviation}}{\text{mean } C_{ht}}\right) \quad (5)$$

Stock fits with hilltop curvature

We fit total SOC, MaOC and POC stocks values with hilltop curvature with the curve function from scipy.optimize in the SciPy package. We used an exponential fit with the form '$a \times$ np.exp($-b \times C_{ht}$)', and r^2 values were calculated with the rscore function from the sklearn package by comparing the predicted values from an exponential decay fits.

Data availability

Soil sample data for figure reconstruction are available within the paper and its Supplementary Information as well as via Figshare[53] (https://doi.org/10.6084/m9.figshare.21816399). LiDAR data for the Rabbit Mountain region in southwestern Oregon for this project are available via the Oregon Department of Geology and Mineral Industries (DOGAMI) online (https://gis.dogami.oregon.gov/maps/lidarviewer/) or through OpenTopography (https://doi.org/10.5069/G9V69GS8)[54].

Code availability

We suggest parties interested in the source code for calculating curvature contact the corresponding author from ref. 37.

References

51. Virtanen, P. et al. SciPy 1.0: fundamental algorithms for scientific computing in Python. *Nat. Methods* **17**, 261–272 (2020).
52. Schwanghart, W. & Scherler, D. Short communication: TopoToolbox 2 – MATLAB-based software for topographic analysis and modeling in Earth surface sciences. *Earth Surf. Dynam.* https://doi.org/10.5194/esurf-2-1-2014 (2014).
53. Hunter, B. D., Roering, J. J., Silva, L. C. R. & Moreland. K. C. Rabbit Mountain soil data. *Figshare* https://doi.org/10.6084/m9.figshare.21816399 (2023).
54. Hunter, B. D. Post-fire debris flow detection and erosion, Oregon 2020. *OpenTopography* https://doi.org/10.5069/G9V69GS8 (NCALM, 2021).

Acknowledgements

Land access to Rabbit Mountain and the Cow Creek recreation area was facilitated through S. Post and K. Knox at the Bureau of Land Management in Roseburg, OR. Soil sample collection sites were approved to avoid culturally sensitive locations. Access to large LiDAR data from DOGAMI was facilitated by J. Edwards. We thank W. Struble for access to curvature code and discussion as well as P. Almond and lab members in the Soil Plant Atmosphere lab group at the University of Oregon for discussions. Thank you to undergraduate students B. Quinn, N. Cleland, D. Kleiner and J. Odenthal, who assisted in soil sample preparation. Funding for this work was provided by NSF Division of Earth Sciences (EAR) Climate grant #2136934 (J.J.R. and L.C.R.S.) and NSF grant #2319597 (L.C.R.S.). Digital elevation model (DEM) data were collected by the National Center for Airborne Laser Mapping (NCALM) as a Seed grant (B.D.H.).

Author contributions

B.D.H. and J.J.R. designed the study and collected samples. L.C.R.S provided access to laboratory equipment and discussion. K.C.M. advised radiocarbon sample preparation and provided discussion. All authors contributed to the interpretation of the results. B.D.H. wrote the paper and produced the figures. J.J.R., L.C.R.S. and K.C.M. provided comments and additions to the text.

Competing interests

The authors declare no competing interests.

Additional information

Extended data is available for this paper at https://doi.org/10.1038/s41561-023-01365-2.

Supplementary information The online version contains supplementary material available at https://doi.org/10.1038/s41561-023-01365-2.

Correspondence and requests for materials should be addressed to Brooke D. Hunter.

Peer review information *Nature Geoscience* thanks Christopher Feeney and Nicholas Patton for their contribution to the peer review of this work. Primary Handling Editor: Xujia Jiang, in collaboration with the *Nature Geoscience* team.

https://doi.org/10.1038/s41561-023-01365-2

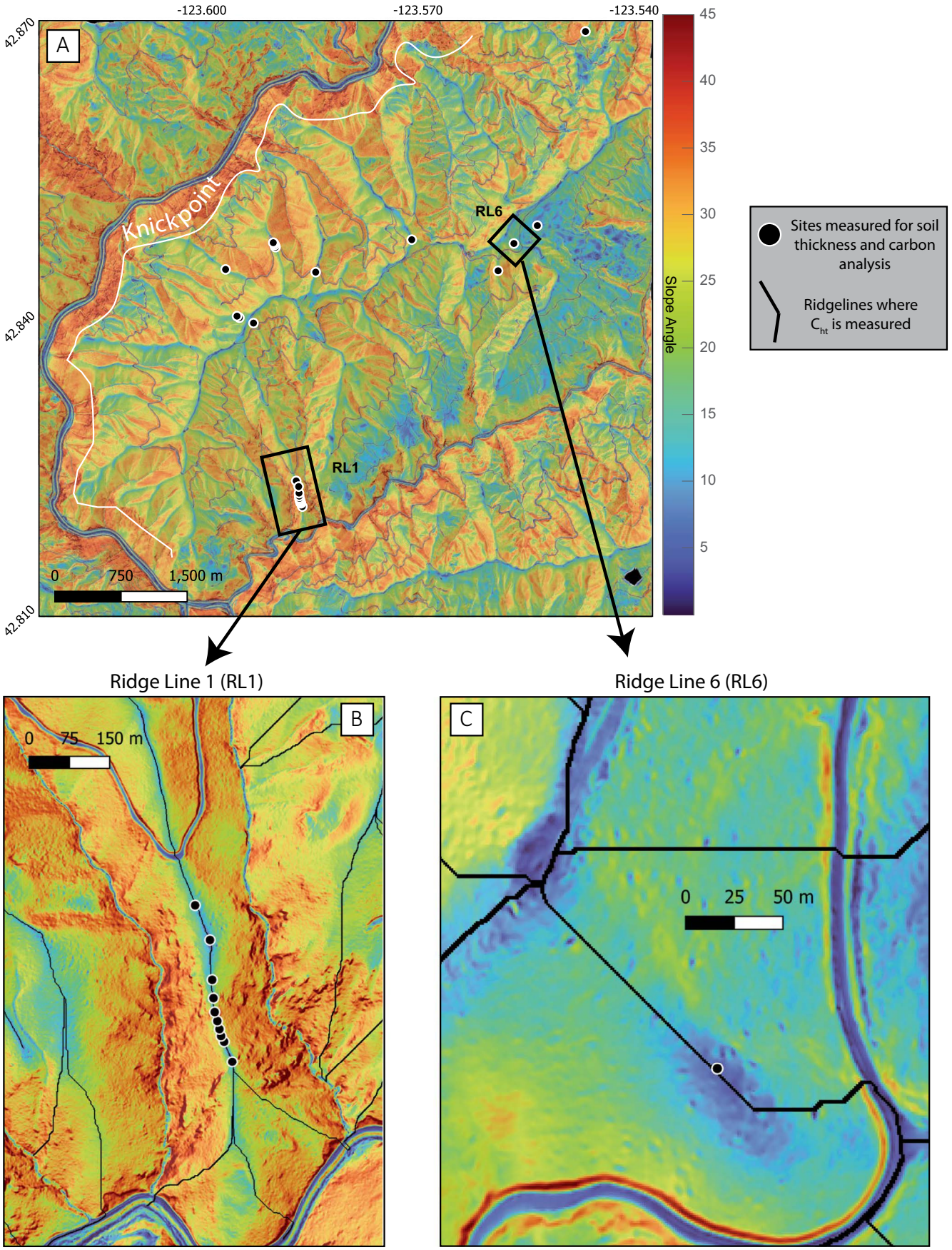

Extended Data Fig. 1 | Field map of Rabbit Mountain with insets. (A), and insets for Ridgeline 1 (RL1) (B), and Ridgeline 6 (RL6) (C). Black dots show locations where we measured soil thickness and collected samples along ridgelines for laboratory analysis. Black lines along ridgelines in (B) and (C) show ridgelines and where we extracted hilltop curvature (C_{ht}) values from full curvature maps.

https://doi.org/10.1038/s41561-023-01365-2

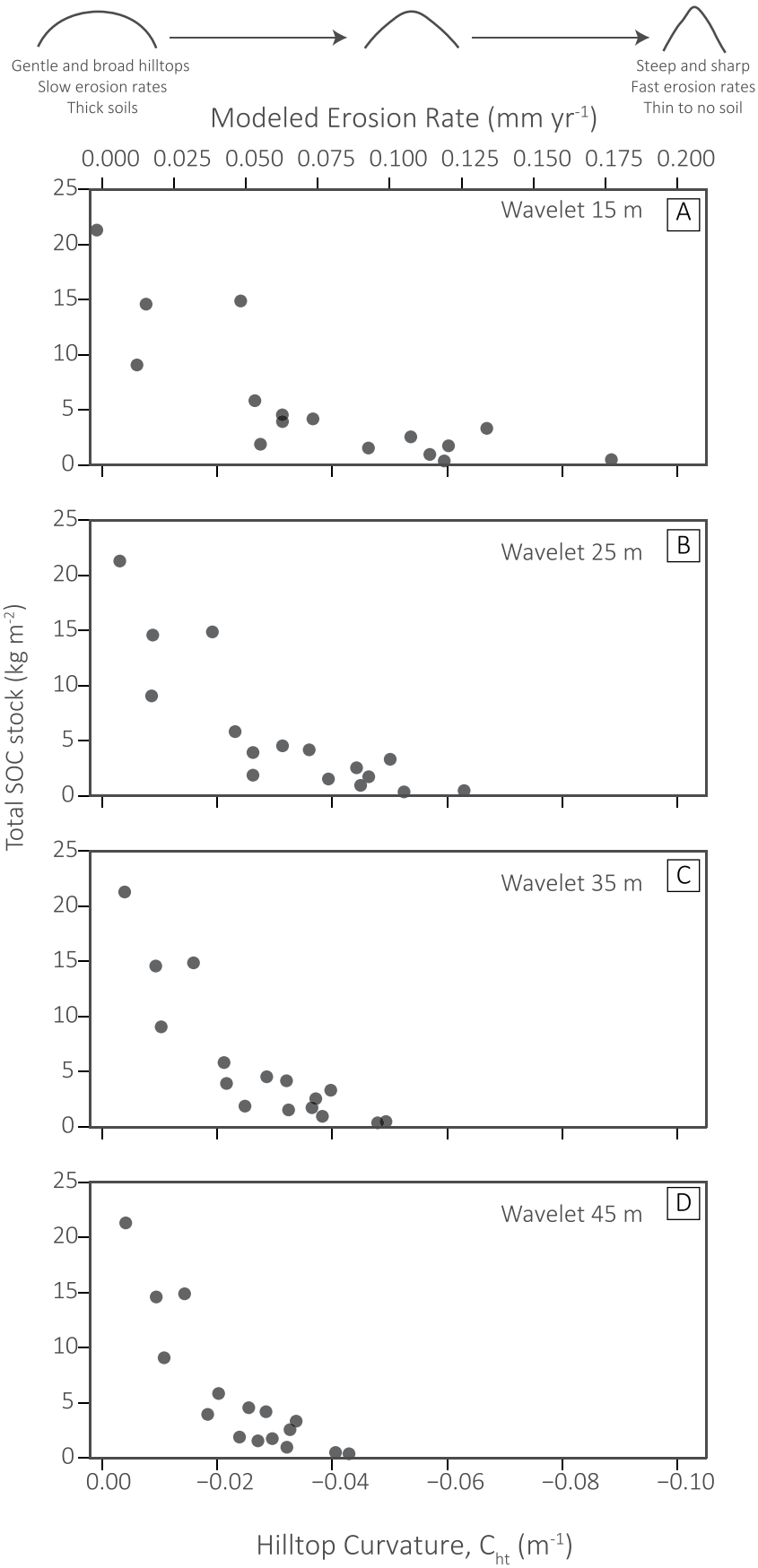

Extended Data Fig. 2 | Total SOC stock with hilltop curvature (Cht) and erosion rate (E) relationships for single wavelet scale across sites. Total SOC (black circles) vs C_{ht} using one single wavelet scale for all sites with selected scales of 15 (A), 25 (B), 35 (C), and 45 (D). The exponential decline in stock trend is present for all scales. The main change is the range of measured curvature values. It is likely that at the 35 and 45 wavelet scales, the fastest (sharpest sites) are underestimated values.

https://doi.org/10.1038/s41561-023-01365-2

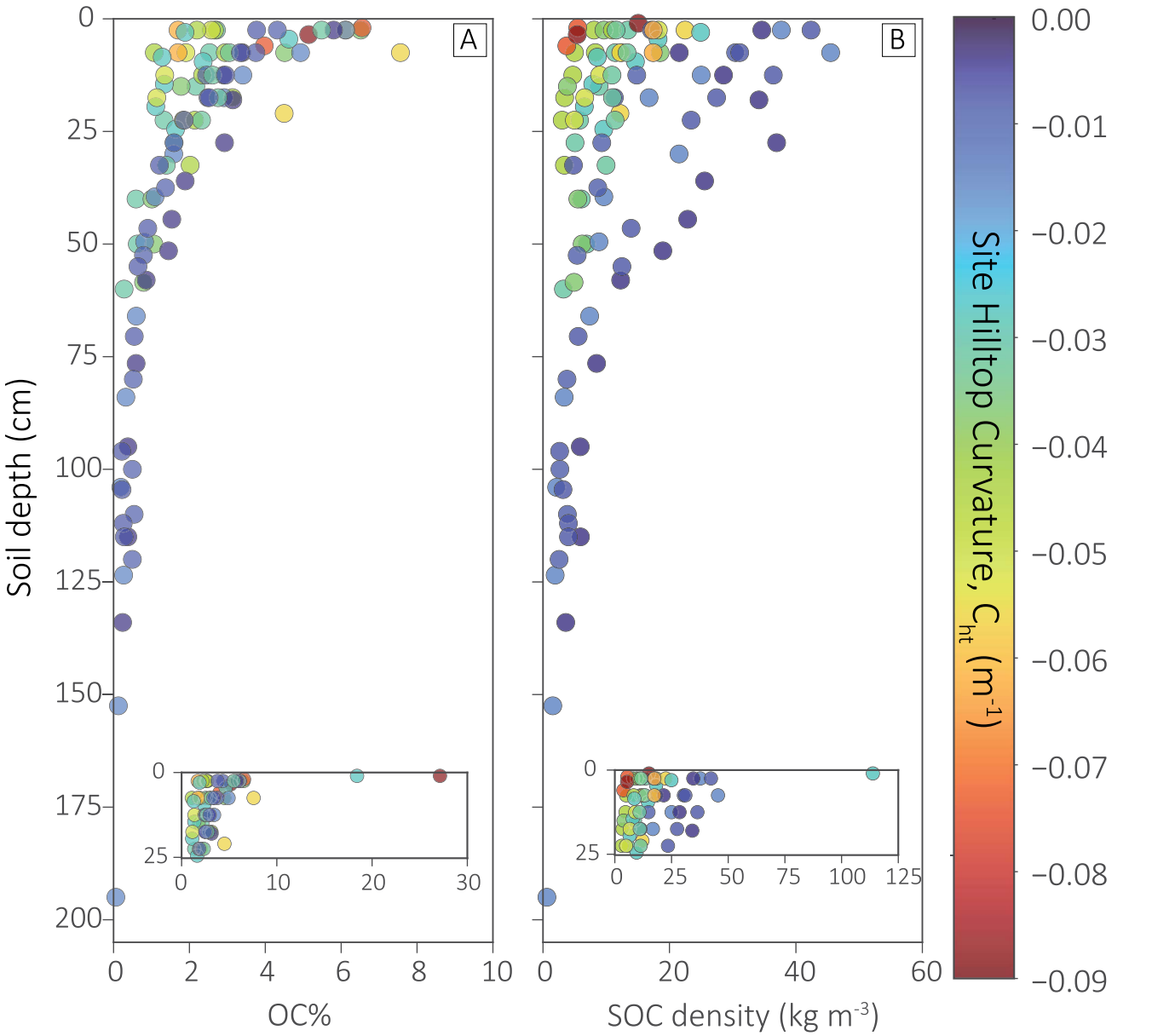

Extended Data Fig. 3 | *OC%* measured on the fine fraction, f_f, of samples. (A) and calculated SOC density (B) values for measured soil samples across all soil depths and site locations. Data are colored by the site's corresponding hilltop curvature, C_{ht}, value A. OC% (percentage of ff mass that is carbon) declines with depth. Inset shows extended x-axis to include two outlier samples with OC% values > 10%. B. SOC density, calculated following Eq. 1, also declines with depth. The incorporation of a coarse fraction mass correction (1 − fc) exemplifies one way soil properties influence SOC density, and thus SOC stock. Slower eroding sites with low C_{ht} values (blue), not only have deeper profiles, but also have SOC density values greater than faster eroding sites (red).

https://doi.org/10.1038/s41561-023-01365-2

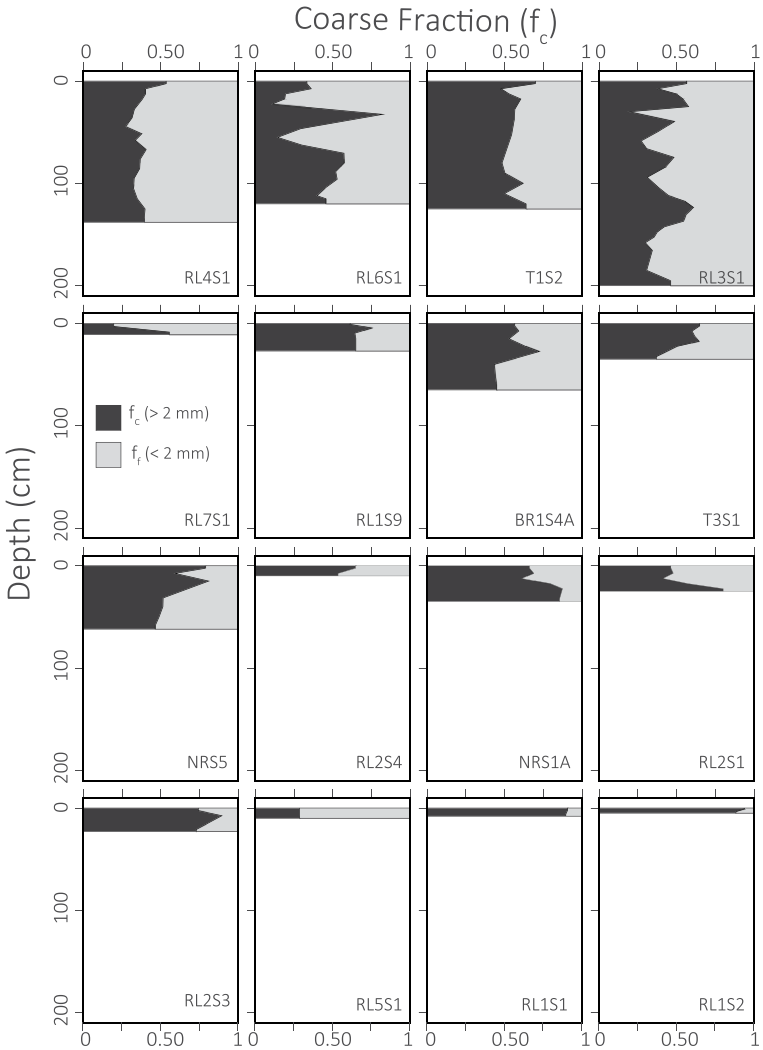

Extended Data Fig. 4 | Coarse, fc (black), and fine, ff (light gray), fraction data with depth for all field sites. Site hilltop curvature (C_{ht}) becomes more convex from top left (C_{ht} = -0.0038 m-1) to bottom right C_{ht} = -0.0855 m-1, and thus modeled erosion rate E increases. Soil profiles become thinner and coarser as fc values increase from ~ 0.36 to 0.90 with faster erosion rates. From field observations, we observed material in the fc also becomes more rounded with slower erosion rates, compared to coarse angular fc material at the fast-eroding sites.

https://doi.org/10.1038/s41561-023-01365-2

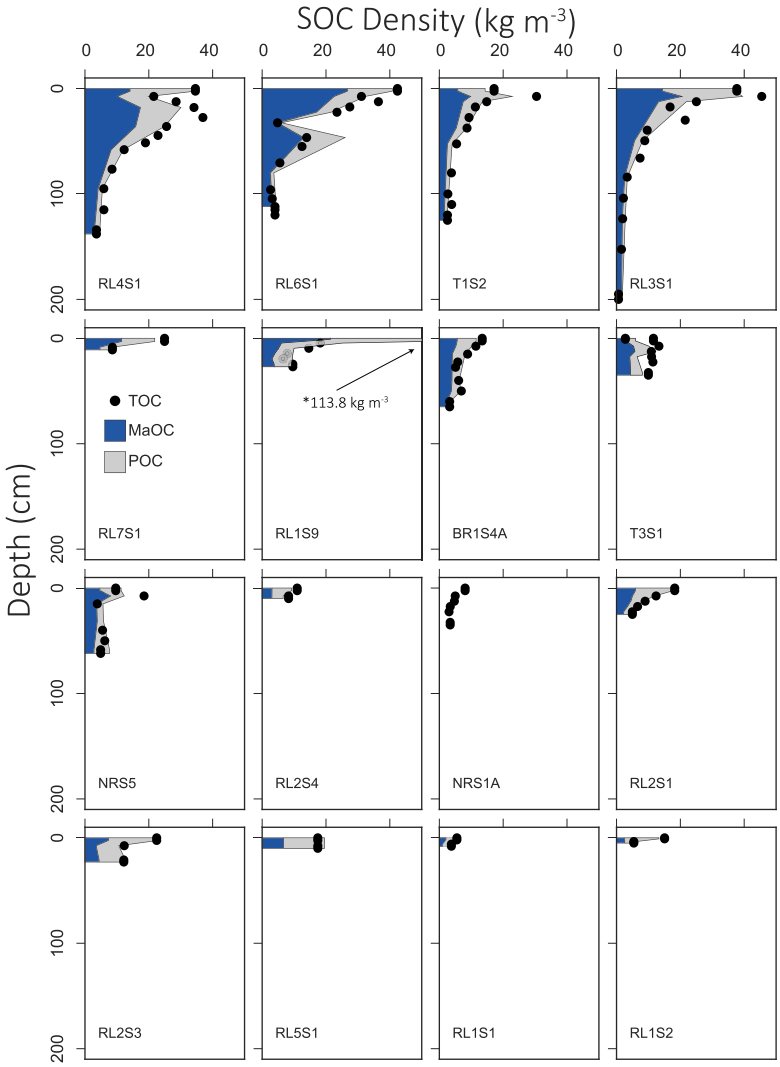

Extended Data Fig. 5 | Organic Carbon Density data with depth. Total SOC (black circles), MaOC (blue), and POC density (gray) decline with depth for each site. Site hilltop curvature (C_{ht}) becomes more convex from top left (C_{ht} = -0.0038 m-1) to bottom right C_{ht} = -0.0855 m-1, and thus modeled erosion rate E increases. Fast eroding sites are dominated by POC fraction, while MaOC dominates at the slower sites. Note site RL9S1 has one outliner off the plot with a value of 113.8 kgm^{-3}.